Communication

Improved Structural Description of Different γ-Al$_2$O$_3$ Materials Using Disordered δ_5-Al$_2$O$_3$ Phase via X-ray Pair Distribution Function Analysis

Fabio Manzoni [1], Benjamin M. D. Fahl [1] and Mirijam Zobel [1,2,*]

[1] Institute of Crystallography, RWTH Aachen University, 52066 Aachen, Germany; manzoni@ifk.rwth-aachen.de (F.M.); benjamin.fahl@rwth-aachen.de (B.M.D.F.)

[2] Jülich Centre for Neutron Science (JCNS-3), Forschungszentrum Jülich GmbH, 52425 Jülich, Germany

[*] Correspondence: author: zobel@ifk.rwth-aachen.de

Abstract: Extensive research has been conducted in the past on the crystallographic characteristics of γ-Al$_2$O$_3$ support materials due to their advantageous properties in heterogeneous catalysis. While their structure is most commonly described as spinel, their intrinsic disorder and nanostructure have prompted alternative models involving tetragonal space groups, supercells, or occupancy of non-spinel positions. X-ray pair distribution function (PDF) analysis has further postulated the existence of short-range order domains with structural remnants from boehmite precursors from which γ-Al$_2$O$_3$ is commonly prepared via calcination. In this PDF study, we now show that a recently theoretically found monoclinic δ_5-Al$_2$O$_3$ phase is, in fact, best suited for describing the structure of different commercial Al$_2$O$_3$ supports, as well as a self-prepared and an industrial Ni/Al$_2$O$_3$ methanation catalyst. Furthermore, in situ experiments under catalytic cycling in the methanation reaction demonstrate that the nanoscale structure of this δ_5 phase is preserved during cycling, pointing towards the high stability of the therein-represented disorder. A complete description of the disordered Al$_2$O$_3$ support structure is crucial in the field of heterogeneous catalysis in order to distinguish disorder within the bulk support from additional interfacial restructuring processes such as surface oxidation or spinel formation due to nanoparticle–support interactions during catalytic cycling in in situ scattering experiments.

Keywords: Al$_2$O$_3$; PDF; crystal structure; heterogeneous catalyst

1. Introduction

In the quest for efficient heterogeneous catalysts, nanostructured γ-Al$_2$O$_3$ has garnered considerable attention as a highly stable support material. Its high industrial relevance is reflected in its usage across various catalytic processes [1–3]. While α-Al$_2$O$_3$ is the thermodynamically most stable modification, its comparably small specific surface of ca. 5 to 20 m^2/g prevents its widespread application [4]. In contrast, γ-Al$_2$O$_3$ features a significantly higher surface area of about 150 to 200 m^2/g, while being stable in temperature ranges of room temperature up to 700 °C, in which many heterogeneously catalyzed reactions can be run [5–7]. Due to this high surface area stemming from the micro- and mesoporosity of γ-Al$_2$O$_3$, catalytically active metal and metal oxide nanoparticles can be stabilized in a well-dispersed state without significant sintering for long periods of time in industrial applications such as the methanation reaction running on Ni/γ-Al$_2$O$_3$ [8,9].

Despite its wide usage, the crystal structure of γ-Al$_2$O$_3$ is still posing a challenge to structural refinements [10–13]. Originally, a cubic spinel structure with partial occupancies of the Al^{3+} cations (see Figure 1b) has been proposed based on the Rietveld analysis of powder X-ray diffraction (PXRD) and neutron diffraction supported by density functional theory (DFT) calculations [14–17]. Yet, the partial occupancies implemented in an average

crystallographic model using a typically sized spinel unit cell (7.9 Å) [18] could not satisfactorily describe the disordered crystal structure of γ-Al$_2$O$_3$ [19]. To account for remaining misfits to the experimental data, tetragonal distortions [20,21] or non-spinel occupancies have been considered [18]. Furthermore, models employing supercells were created, which contained different stacking faults or antiphase boundaries [17]. An alternate description of the γ-Al$_2$O$_3$ structure was then suggested using a *c*-symmetry-based tetragonal model in space group I4$_1$/amd; see Figure 1a [22]. Since γ-Al$_2$O$_3$ is prepared from boehmite precursors via calcination, various studies have additionally pointed out that the actual γ-Al$_2$O$_3$ structure is highly dependent on the precursor structure and the history of thermal treatment [19,23].
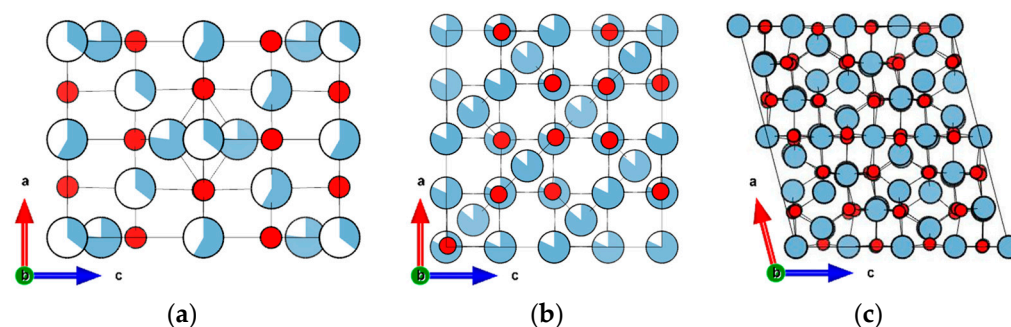

(a)   (b)   (c)

Figure 1. Crystal structures of the (**a**) tetragonal, (**b**) spinel, and (**c**) δ$_5$ phases of Al$_2$O$_3$ (from left to right), shown as projections into the ac plane. Oxygen atoms in red, aluminum atoms in blue, with partial occupancies indicated with partially filled blue circles.

With the rise of the pair distribution function (PDF) analysis of high-energy X-ray scattering data in the field of nanostructured materials [24], the structure of γ-Al$_2$O$_3$ has been revisited. The PDF, labeled $G(r)$, can be understood as a histogram of the interatomic distances r_{ij} between the atoms i and j in the sample and is thus highly suited for structurally characterizing disordered materials:

$$G(r) = \frac{1}{Nr} \sum_{i,j} \left[\frac{f_i(Q)f_j(Q)}{\langle f(Q) \rangle^2} \delta(r - r_{ij}) \right] - 4\pi r \rho_0 \tag{1}$$

The interatomic distances are weighted by the scattering powers of the two contributing atoms, i.e., the X-ray atomic form factor $f_i(Q)$ for atom i, and the average scattering length of all atoms $\langle f(Q) \rangle^2$, taking into account the atomic number density ρ_0 and the total number of atoms N in the sample [25]. Experimentally, the PDF is gained by Fourier transformation of PXRD data over very large scattering angles. Hereby, this technique not only exploits the scattering from within the Bragg peaks but also exploits any diffuse scattering in between and below the Bragg peaks, which contains further information about the disorder. Using PDF analysis, Paglia et al. extended their previous tetragonal model of the average structure of γ-Al$_2$O$_3$ [22] by showing that the short-range structure of γ-Al$_2$O$_3$ deviates from the average one [19]. The local structure extends about 1 nm and was explained by stacking faults in the oxygen sublattice, being a remnant of the precursor structure boehmite [19,22].

Operando PXRD and PDF measurements of catalytic cycling are becoming increasingly popular to derive structure–activity relationships since the PDF can be used to track the structure and particle size of the catalyst particles, as well as simultaneously access the structure of the support material—even with subsecond time resolution at modern synchrotron radiation facilities [26–28]. Simultaneously, the detection and interpretation of ever smaller signals and so-far non-described structural residuals in refinements become ever more important for catalyst design in light of metal–support interactions, for instance.

Various PDF refinements on different γ-Al$_2$O$_3$ structures using the improved tetragonal model achieved by Paglia et al. [19] feature different degrees of structural residuals in the different curves of the fits. These residuals have been reasoned, for instance, with slightly different γ-Al$_2$O$_3$ structures due to the different calcination procedures of boehmite precursors or with interfacial restructuring of the γ-Al$_2$O$_3$ [8,29]. Yet, so far, an improved structural description has remained out of reach.

Very recently, for γ-Al$_2$O$_3$, Kovarik et al. found co-existing spinel and δ-Al$_2$O$_3$ domains in transmission electron microscopy (TEM) images, which supported previous ideas that γ-Al$_2$O$_3$ contains several crystallographic domains (twins, stacking faults, supercells) [30]. In earlier works, they had already investigated samples of δ-Al$_2$O$_3$ only and found them to be an intricate intergrowth of closely related polymorphs within the δ-Al$_2$O$_3$ family. These intergrowth structures had been visualized by scanning TEM (STEM) and called δ_1, δ_2, δ_3, and δ_4—complemented by a δ_5 phase obtained by DFT calculation [31–33]. Those phases feature differences in their symmetry (space groups $P2_12_12_1$, $P2_1$, $A2/n$, P-1, and $A2$, respectively), the number of atoms per unit cell, and the lattice parameters (see Figure S1 and Table S4).

In this study, we now employed these δ phases to refine experimental PDF data of different γ-Al$_2$O$_3$ supports and methanation catalysts. Herein, we show that, in many cases, catalysts are assumed to be built upon the γ-Al$_2$O$_3$ but feature a δ_5-crystal structure instead.

2. Results and Discussion

2.1. Improved Description of γ-Al$_2$O$_3$ Materials with δ_5 Phase

To improve the structural description of Al$_2$O$_3$ materials in PDF refinements, we compared the fit quality of different crystal structures to several Al$_2$O$_3$ materials, which are commercially available as γ-Al$_2$O$_3$: the most widely used spinel structure [18], the tetragonal model [22], and the recently established five intergrowth δ phases found by Kovarik et al. [31]. Figure 2 shows the PDF refinements of the Al$_2$O$_3$ support labeled as SBa200 by Sasol, Hamburg, Germany, being widely employed in catalysis for its high surface area, and Figure S7 compares the experimental PXRD pattern of SBa200 with the simulated PXRD patterns of these three crystallographic phases. The spinel phase describes the Al$_2$O$_3$ structure slightly better than the tetragonal phase in the PDF refinement, which is evidenced by the lower goodness-of-fit parameter R_w of 0.23 for the spinel compared to 0.25 for the tetragonal phase (for details on R_w calculation, see Section 3). For both phases, though, the short-range order for interatomic distances < 15 Å is not well described and shows higher residuals than the average noise level in the data in the difference curves, which is highlighted in Figure 2 by the boxes with dashed lines in the difference curves. The result values of all fit parameters for SBa200 are contained in Table S5, and the corresponding refinements for the supports SBa150 and TH100-150 by Sasol are shown in Figure S2 in the Supplementary Materials.

Fitting the five different δ phases to the experimental PDF of SBa200, phase δ_4 did not describe the data at all. The phases δ_1 and δ_2 fit the data slightly worse or had a similar goodness of fit as the spinel and tetragonal structures, and δ_3 improves the fit quality slightly. The monoclinic δ_5 phase described the PDF and, in particular, the short-range order < 20 Å the best and better than the spinel model, as shown in Figure 2c, yielding a goodness-of-fit R_w = 0.18. The δ_5 phase yielded the overall best-fit results for the supports SBa150 and TH100-150, too. Comparing the resulting fit values for B$_{iso}$(O) and B$_{iso}$(Al) for the spinel, tetragonal, and δ_5 phase shows that the values are larger for the spinel and tetragonal structure. Both static disorder and thermal disorder can contribute to peak broadening in the PDF; the higher the disorder or thermal motion, the higher the B$_{iso}$ value. Given the higher static disorder with off-centered atomic positions in the δ_5 phase, the B$_{iso}$ values for the spinel and tetragonal structure likely do not reflect higher thermal motion but try to make up for structural disorder, which is not included in the crystal structure of the spinel and tetragonal models.
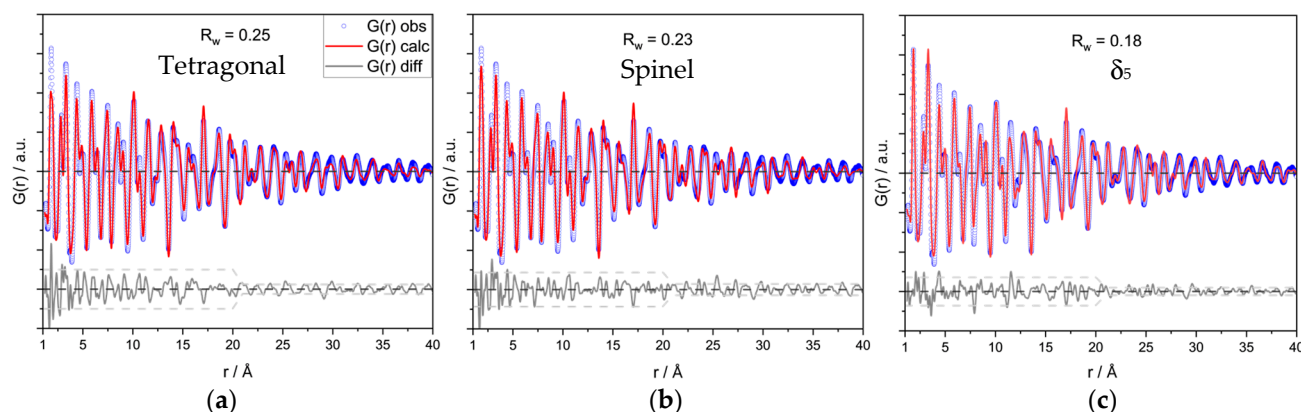
Figure 2. Refinements of the experimental PDF, $G(r)$, for the Al_2O_3 support SBa200 by using the (**a**) tetragonal, (**b**) spinel, and (**c**) δ_5 structures. Experimental PDF data, $G(r)$ obs, in blue circles, fitted calculated PDF, $G(r)$ calc, as red line, and the difference curve in grey in offset, with the goodness-of-fit R_w in each panel. Boxes in dashed lines around difference curves indicate the standard deviation of data points over the short range up to 20 Å and the medium range > 20 Å.

The mismatch of the local structure with the spinel or tetragonal models was addressed before in the PDF study by Paglia et al. [19], where they proposed fitting a P1 structure to the local order from 1.2 to 8 Å in addition to the average tetragonal structure. This P1 model is highly parametrized, though. To prevent fits resulting in too-short bond lengths upon refinement of the atomic xyz positions, we did not refine the xyz positions and employed 17 parameters. Those refinements shown in Figure S3 did not improve the fit quality compared to fits using the δ_5 phase.

Hence, this comparison of different crystal structures to the experimental PDF data of commercial γ-Al_2O_3 suggests that the crystal structure of what is referred to as a commercial γ-Al_2O_3 is, in fact, a monoclinic δ_5 phase.

2.2. Supported Catalysts—Ni/Al₂O₃

The industrially employed Ni/Al_2O_3 methanation catalyst labeled SPP2080-IMRC has recently been investigated in a multi-method approach to establish a holistic description, to which we have contributed PDF characterization [8]. The PDF experiments were carried out in situ during reducing conditions (i.e., during catalyst activation). After activation, the nickel species exist as nanoparticles with face-centered cubic lattice (Ni_{fcc}). To structurally describe the experimental PDF, the fits consist of two phases: a Ni_{fcc} phase with a refinable particle diameter and an Al_2O_3 phase being either the tetragonal, the spinel, or the δ_5 phase, as shown in Figure 3a–c. For all three fits, the nanoparticle diameter and Ni_{fcc} lattice parameter were refined to similar values of 2.3 nm and 3.54 Å. On the contrary, the fit qualities differed for the three Al_2O_3 phases, which was again best described by the δ_5 phase. The residual curve of the δ_5 phase clearly shows less structural signal in Figure 3c. For the catalyst before activation, the Ni_{fcc} phase was replaced by a NiO phase, but the δ_5 phase very robustly also gave the best-fit results there, as shown in Figure S4.

In the original publication on the characterization of the SPP2080-IMRC Ni/Al_2O_3 catalyst [8], the unknown Al_2O_3 phase was optimized starting from a spinel structure with additional Al^{3+} ions on non-spinel positions to take into account some disorder. Yet, the short-range order could not be well described, and the goodness of fit remained worse, at $R_w = 0.31$, than that found here with the δ_5 phase.

To investigate the phase stability of the δ_5 phase during catalytic operation conditions as impinged by a renewable energy supply, we performed in situ methanation experiments on a model Ni/Al_2O_3 catalyst at beamline ID15, ESRF. This catalyst with 15 wt% Ni on the SBa200 support was cycled between catalysis (H_2:CO_2 = 4:1) and hydrogen dropouts at 425 °C four times over a total of 4 h in a flow cell reactor after activation in pure hydrogen

(see Methods for details of in situ experiment). Hydrogen dropouts mimic the shortage of hydrogen in an industrial scenario when hydrogen is produced from electrocatalytic water splitting via renewable energies, which undergo fluctuations (sun, wind) [34]. The biphasic PDF refinements of the Ni_{fcc} nanoparticle and the δ_5 phase revealed that the δ_5 phase is structurally stable. The average domain size of the δ_5 phase increases only slightly during the catalytic cycling by ca. 60 Å to 69 Å, as shown Figure S5a, which is insignificant growth given the spread of data points and having an interatomic Al-O bond length of 1.82 Å in the tetrahedral sites and 1.90 Å for the octahedral sites. This shows that the nanoscale structure of the δ_5 phase is preserved under catalytic cycling, pointing towards the high stability of the therein-represented nanostructured motifs and distortions.
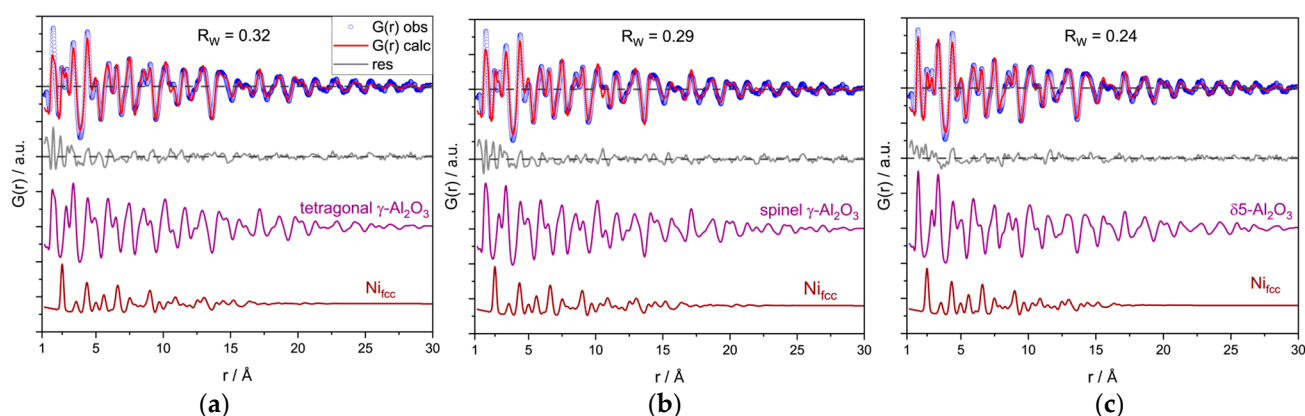

Figure 3. Refinement of experimental PDF data of an industrial methanation catalyst Ni/Al_2O_3 using two phases, with one phase being Ni_{fcc} nanoparticles and the second being the (**a**) tetragonal, (**b**) spinel, and (**c**) δ_5 phases for describing Al_2O_3 support. Experimental PDF data, *G*(*r*) obs, in blue circles, fitted calculated PDF, *G*(*r*) calc, as red line, and the difference curve in grey in offset, with the goodness-of-fit R_w in each panel. The contribution of the two phases to the total fit curve is shown in the offset: in purple for Al_2O_3 and in brown for Ni_{fcc}.

3. Experimental Section

3.1. Synthesis of Ni/Al₂O₃

The support materials of the nominally γ-Al_2O_3 structures called SBa200, SBa150, and TH100-150 were provided by Sasol, Hamburg, Germany. These supports differ in surface area and porosity; see Table S6 and Figure S8 in the Supplementary Materials. These support materials were used without further purification or treatment for the preparation of Ni/γ-Al_2O_3 catalysts following a urea precipitation method according to Grunwaldt et al. [9]: Urea was added under constant stirring into a $Ni(NO_3)_2$ water solution to yield a molar ratio of urea: Ni = 2:1 at room temperature. An Al_2O_3 water suspension (1.6 g Al_2O_3 in 50 mL water) was added, and the reaction was run for 48 h at 90 °C while constantly stirring. The green precipitate was washed with water and dried overnight in an oven at 90 °C, and the resulting powder was calcined at 400 °C for 3 h.

3.2. Characterization

Surface area and porosity measurements of the three supports SBa200, SBa150, and TH100-150 were performed with the BET-BJH method by adsorption of N_2 (assuming 16.2 $Å^2$ as the area of a N_2 molecule) at the temperature of liquid nitrogen after outgassing the samples at 400 °C for 2 h. The instrument used for this analysis was the 3P macro 200C, 3P Instruments, Odelzhausen, Germany, and the results are shown in Figure S8.

The industrial methanation catalyst of the SPP2080, Ni/Al_2O_3, labeled SPP2080-IMRC, was previously thoroughly characterized by Weber et al. [8]. This catalyst features 8.6 wt% Ni.

3.3. X-ray Total Scattering Experiments

Synchrotron: Total scattering data of the powder samples were acquired at the ID15A beamline at the ESRF (Grenoble, France) with an X-ray energy of 65 keV (λ = 0.1907 Å) and a beam size of 150 × 150 μm^2 in quartz capillaries with a diameter of 1 mm. Every data set was collected for 1 s with a Pilatus CdTe 2M detector (DECTRIS, Baden-Daettwil, Switzerland). Radial integration was performed with the software xpdtools, version 0.8 [35] and PDF calculation with PDFgetX3, version 2.2.1 [36] using a Q_{max} of 24 Å^{-1}. The instrumental resolution was determined from a LaB$_6$ standard with q_{damp} = 0.02 and q_{broad} = 0.009.

In situ catalysis experiment at synchrotron: These in situ experiments were carried out in a custom-built quartz capillary reactor (outer diameter 1.5 mm, wall thickness 0.05 mm) with heating coils for temperature control and a gas dosing system with mass flow controllers (Bronkhorst, AK Ruurlo, The Netherlands) to adjust the gas flow of He, H$_2$, and CO$_2$, with an overall gas flow of 10 mL min^{-1}, while using a catalyst amount of 7–10 mg. The catalytic and dropout cycles were alternated every 30 min. Data were measured continuously with 1 s for each detector image and 29 s sleep time after each image to prevent ghosting issues on the Pilatus CdTe 2M detector.

Industrial methanation catalyst SPP2080-IMRC: For PDF data collection and processing of the industrial methanation catalyst SPP2080-IMRC, see Weber et al. [8].

3.4. PDF Modeling

PDF refinements were conducted with Diffpy-CMI, version 3.0 [37]. All data sets were fit over a range of 1–80 Å for comparability of fit results between the different supports. For all refinements, first, the lattice parameter(s) and scale were refined, then the domain size and shape parameters of the characteristic functions for the spherical nanoparticles, followed by the atomic isotropic atomic displacement parameter B_{iso} and the parameter $\delta2$ for the correlated atomic motion of nearest neighbors. Finally, occupancies were freed, if included in the model. The fractional atomic coordinates xyz were not fitted to prevent overfitting and unphysical bond distances.

The goodness of fit is defined by Equation (2), where $G_{obs}(r)$ and $G_{calc}(r)$ are the observed and modeled PDFs, $w(r_r)$ is the weighting factor of each data point I, and s is the scale factor of the model to the data [38].

$$R_w = \left\{ \frac{\sum_i w(r_i) [G_{obs}(r_i) - sG_{calc}(r_i)]^2}{\sum_i w(r_i) [G_{obs}(r_i)]^2} \right\}^{1/2} \tag{2}$$

For the spinel phase, 10 parameters were refined: lattice parameter *a*, domain size, scale, $\delta2$, and $B_{iso}(O)$. For the four Al sites, one occupancy was refined for each, while their four B_{iso} parameters were combined into a single parameter $B_{iso}(Al)$. The tetragonal phase was refined with 10 parameters: lattice parameters *a* and *c*, domain size, scale, $\delta2$, and $B_{iso}(O)$. Again, the B_{iso} of the three Al sites was combined. The oxygen occupancies were not refined, but the three Al ones were. For both spinel and tetragonal models, the oxygen occupancies were not refined, and the resulting elemental ratio Al:O was crosschecked to be close to the nominal Al$_2$O$_3$ composition upon Al occupancy refinement.

The local structure, according to the Paglia model, was fitted with a P1 phase for 1.2 < r < 8 Å, refining lattice parameters *a*, *b*, and *c*; domain size; scale; $\delta2$; and individual $B_{iso}(O)$ and $B_{iso}(Al)$ for each atom, resulting in 17 parameters.

For the δ_5 phase, 9 parameters were used: lattice parameters *a*, *b*, and *c*; angle β; domain size; scale; $\delta2$; $B_{iso}(Al)$; and $B_{iso}(O)$. Since the δ_5 phase has 42 Wyckoff sites, we used one B_{iso} value for all atom sites of one element. Partial occupancies and xyz positions were not refined for any site.

For refining the in situ data, the fit results of one data set were used as the starting point for the subsequent data set. Additionally, when fit results showed a phase to be <5% of the summed scale, the fit of this data set was repeated without this phase. The value of

5% was chosen because this was the threshold where the fit was able to describe the data, and, for phase fractions < 5%, these phases merely fitted noise.

4. Conclusions

Understanding the structure of a disordered support material, such as γ-Al_2O_3, is essential for deducing structure–activity correlations and achieving ultimate insight into particle–support interactions, for instance. In this study, the power of PDF analysis for characterizing nanostructured materials was highlighted again in the field of heterogeneous catalysis. For different commercial Al_2O_3 supports, as well as a self-prepared and an industrial Ni/Al_2O_3 methanation catalyst, we obtained a superior structural description using a recently found monoclinic δ_5 phase compared to the established spinel and tetragonal models. Furthermore, the δ_5 structure remained stable during catalytic cycling, which proves the robustness of this nanostructure against restructuring. Although, pretty commonly, various Al_2O_3 supports have been associated and labeled as being γ-Al_2O_3, this PDF study of their local structure revealed that the structure of a significant number of Al_2O_3 supports is actually better described by the δ_5 phase and could, thus, better be called δ_5-Al_2O_3 in the future. More importantly, though, in order to improve the structural characterization of catalytic systems for enhanced structure–activity correlations, we hope that this improved δ_5 structure finds its way into databanks and broad application across communities soon. A complete description of the disordered Al_2O_3 support structure is crucial to the field of heterogeneous catalysis in order to distinguish general disorder within the bulk support from additional interfacial restructuring processes upon catalyst loading or during catalyst cycling, such as surface oxidation or spinel formation due to nanoparticle-support interactions.

References

1. Busca, G.; Spennati, E.; Riani, P.; Garbarino, G. Looking for an Optimal Composition of Nickel-Based Catalysts for CO_2 Methanation. *Energies* **2023**, *16*, 5304. [CrossRef]
2. Hu, F.; Ye, R.; Lu, Z.-H.; Zhang, R.; Feng, G. Structure–Activity Relationship of Ni-Based Catalysts toward CO_2 Methanation: Recent Advances and Future Perspectives. *Energy Fuels* **2022**, *36*, 156–169. [CrossRef]
3. Lee, Y.H.; Ahn, J.Y.; Nguyen, D.D.; Chang, S.W.; Kim, S.S.; Lee, S.M. Role of oxide support in Ni based catalysts for CO_2 methanation. *RSC Adv.* **2021**, *11*, 17648–17657. [CrossRef]
4. Rascón, F.; Wischert, R.; Copéret, C. Molecular nature of support effects in single-site heterogeneous catalysts: Silica vs. *alumina.*. *Chem. Sci.* **2011**, *2*, 1449. [CrossRef]

5. Candia, R.; Sørensen, O.; Villadsen, J.; Topsøe, N.Y.; Clausen, B.S.; Topsøe, H. Effect of Sulfiding Temperature on Activity and Structures of CO-MO/Al$_2$O$_3$ Catalysts. ii. *Bull. Sociétés Chim. Belg.* **1984**, *1984*, 763–774. [CrossRef]

6. Zhang, J.; Xu, H.; Jin, X.; Ge, Q.; Li, W. Characterizations and activities of the nano-sized Ni/Al$_2$O$_3$ and Ni/La–Al$_2$O$_3$ catalysts for NH3 decomposition. *Appl. Catal. A Gen.* **2005**, *290*, 87–96. [CrossRef]

7. Centeno, M.A.; Hadjiivanov, K.; Venkov, T.; Klimev, H.; Odriozola, J.A. Comparative study of Au/Al$_2$O$_3$ and Au/CeO$_2$-Al$_2$O$_3$ catalysts. *J. Mol. Catal. A Chem.* **2006**, *252*, 142–149. [CrossRef]

8. Weber, S.; Zimmermann, R.T.; Bremer, J.; Abel, K.L.; Poppitz, D.; Prinz, N.; Ilsemann, J.; Wendholt, S.; Yang, Q.; Pashminehazar, R.; et al. Digitization in Catalysis Research: Towards a Holistic Description of a Ni/Al$_2$O$_3$ Reference Catalyst for CO$_2$ Methanation. *ChemCatChem* **2022**, *14*, e202101878. [CrossRef]

9. Mutz, B.; Gänzler, A.; Nachtegaal, M.; Müller, O.; Frahm, R.; Kleist, W.; Grunwaldt, J.-D. Surface Oxidation of Supported Ni Particles and Its Impact on the Catalytic Performance during Dynamically Operated Methanation of CO$_2$. *Catalysts* **2017**, *7*, 279. [CrossRef]

10. Prins, R. Location of the Spinel Vacancies in γ-Al$_2$O$_3$. *Angew. Chem. Int. Ed Engl.* **2019**, *58*, 15548–15552. [CrossRef]

11. Prins, R. On the structure of γ-Al$_2$O$_3$. *J. Catal.* **2020**, *392*, 336–346. [CrossRef]

12. Samain, L.; Jaworski, A.; Edén, M.; Ladd, D.M.; Seo, D.-K.; Javier Garcia-Garcia, F.; Häussermann, U. Structural analysis of highly porous γ-Al$_2$O$_3$. *J. Solid State Chem.* **2014**, *217*, 1–8. [CrossRef]

13. Sun, M.; Nelson, A.E.; Adjaye, J. Examination of spinel and nonspinel structural models for gamma-Al$_2$O$_3$ by DFT and rietveld refinement simulations. *J. Phys. Chem. B* **2006**, *110*, 2310–2317. [CrossRef] [PubMed]

14. Verwey, E.J.W. The Crystal Structure of γ-Fe$_2$O$_3$ and γ-Al$_2$O$_3$. *Z. Für Krist.-Cryst. Mater.* **1935**, *91*, 65–69. [CrossRef]

15. Ushakov, V.A.; Moroz, E.M. Structure of low-temperature γ- and η-Al$_2$O$_3$. *React. Kinet. Catal. Lett.* **1984**, *24*, 113–118. [CrossRef]

16. Zhou, R.-S.; Snyder, R.L. Structures and transformation mechanisms of the η, γ and θ transition aluminas. *Acta Crystallogr. Sect. B Struct. Sci.* **1991**, *47*, 617–630. [CrossRef]

17. Rudolph, M.; Motylenko, M.; Rafaja, D. Structure model of γ-Al$_2$O$_3$ based on planar defects. *IUCrJ* **2019**, *6*, 116–127. [CrossRef] [PubMed]

18. Smrcok, L.; Langer, V.; Krestan, J. Gamma-alumina: A single-crystal X-ray diffraction study. *Acta Crystallogr. C* **2006**, *62*, i83–i84. [CrossRef] [PubMed]

19. Paglia, G.; Božin, E.S.; Billinge, S.J.L. Fine-Scale Nanostructure in γ-Al$_2$O$_3$. *Chem. Mater.* **2006**, *18*, 3242–3248. [CrossRef]

20. Saalfeed, H. The Dehydration of Gibbsite and the Structure of a Tetragonal γ-Al$_2$O$_3$. *Clay Miner.* **1958**, *3*, 249–257. [CrossRef]

21. Wilson, S.J. The dehydration of boehmite, γ-AlOOH, to γ-Al$_2$O$_3$. *J. Solid State Chem.* **1979**, *30*, 247–255. [CrossRef]

22. Paglia, G.; Buckley, C.E.; Rohl, A.L.; Hunter, B.A.; Hart, R.D.; Hanna, J.V.; Byrne, L.T. Tetragonal structure model for boehmite-derived γ-alumina. *Phys. Rev. B* **2003**, *68*, 144110. [CrossRef]

23. Xie, Y.; Kocaefe, D.; Kocaefe, Y.; Cheng, J.; Liu, W. The Effect of Novel Synthetic Methods and Parameters Control on Morphology of Nano-alumina Particles. *Nanoscale Res. Lett.* **2016**, *11*, 259. [CrossRef] [PubMed]

24. Billinge, S.J.L.; Kanatzidis, M.G. Beyond crystallography: The study of disorder, nanocrystallinity and crystallographically challenged materials with pair distribution functions. *Chem. Commun.* **2004**, 749–760. [CrossRef]

25. Billinge, S.J.L. Nanostructure studied using the atomic pair distribution function. *Z. Kristallogr. Suppl.* **2007**, *26*, 17–26. [CrossRef]

26. Newton, M.A.; Di Michiel, M.; Ferri, D.; Fernàndez-Garcia, M.; Beale, A.M.; Jacques, S.D.M.; Chupas, P.J.; Chapman, K.W. Catalytic Adventures in Space and Time Using High Energy X-rays. *Catal Surv Asia* **2014**, *18*, 134–148. [CrossRef]

27. Zimmerli, N.K.; Müller, C.R.; Abdala, P.M. Deciphering the structure of heterogeneous catalysts across scales using pair distribution function analysis. *Trends Chem.* **2022**, *4*, 807–821. [CrossRef]

28. Chupas, P.J.; Chapman, K.W.; Chen, H.; Grey, C.P. Application of high-energy X-rays and Pair-Distribution-Function analysis to nano-scale structural studies in catalysis. *Catal. Today* **2009**, *145*, 213–219. [CrossRef]

29. Schlicher, S.; Prinz, N.; Bürger, J.; Omlor, A.; Singer, C.; Zobel, M.; Schoch, R.; Lindner, J.K.N.; Schünemann, V.; Kureti, S.; et al. Quality or Quantity? How Structural Parameters Affect Catalytic Activity of Iron Oxides for CO Oxidation. *Catalysts* **2022**, *12*, 675. [CrossRef]

30. Kovarik, L.; Bowden, M.; Khivantsev, K.; Kwak, J.H.; Szanyi, J. Structural complexity of γ-Al$_2$O$_3$: The nature of vacancy ordering and the structure of complex antiphase boundaries. *Acta Mater.* **2024**, *266*, 119639. [CrossRef]

31. Kovarik, L.; Bowden, M.; Shi, D.; Szanyi, J.; Peden, C.H.F. Structural Intergrowth in δ-Al$_2$O$_3$. *J. Phys. Chem. C* **2019**, *123*, 9454–9460. [CrossRef]

32. Kovarik, L.; Bowden, M.; Shi, D.; Washton, N.M.; Andersen, A.; Hu, J.Z.; Lee, J.; Szanyi, J.; Kwak, J.-H.; Peden, C.H.F. Unraveling the Origin of Structural Disorder in High Temperature Transition Al$_2$O$_3$: Structure of θ-Al$_2$O$_3$. *Chem. Mater.* **2015**, *27*, 7042–7049. [CrossRef]

33. Kovarik, L.; Bowden, M.; Genc, A.; Szanyi, J.; Peden, C.H.F.; Kwak, J.H. Structure of δ-Alumina: Toward the Atomic Level Understanding of Transition Alumina Phases. *J. Phys. Chem. C* **2014**, *118*, 18051–18058. [CrossRef]

34. Kalz, K.F.; Kraehnert, R.; Dvoyashkin, M.; Dittmeyer, R.; Gläser, R.; Krewer, U.; Reuter, K.; Grunwaldt, J.-D. Future Challenges in Heterogeneous Catalysis: Understanding Catalysts under Dynamic Reaction Conditions. *ChemCatChem* **2017**, *9*, 17–29. [CrossRef] [PubMed]

35. Wright, C.J.; Zhou, X.D. Computer-assisted area detector masking. *J. Synchrotron Radiat.* **2017**, *24*, 506–508. [CrossRef] [PubMed]

36.   Juhás, P.; Davis, T.; Farrow, C.L.; Billinge, S.J.L. PDFgetX3: A rapid and highly automatable program for processing powder diffraction data into total scattering pair distribution functions. *J. Appl. Crystallogr.* **2013**, *46*, 560–566. [CrossRef]

37.   Juhás, P.; Farrow, C.L.; Yang, X.; Knox, K.R.; Billinge, S.J.L. Complex modeling: A strategy and software program for combining multiple information sources to solve ill posed structure and nanostructure inverse problems. *Acta Crystallogr. A Found. Adv.* **2015**, *71*, 562–568. [CrossRef] [PubMed]

38.   Peterson, P.F.; Božin, E.S.; Proffen, T.; Billinge, S.J.L. Improved measures of quality for the atomic pair distribution function. *J. Appl. Crystallogr.* **2003**, *36*, 53–64. [CrossRef]

39.   Macrae, C.F.; Sovago, I.; Cottrell, S.J.; Galek, P.T.A.; McCabe, P.; Pidcock, E.; Platings, M.; Shields, G.P.; Stevens, J.S.; Towler, M.; et al. Mercury 4.0: From visualization to analysis, design and prediction. *J. Appl. Crystallogr.* **2020**, *53*, 226–235. [CrossRef]